

Visualizing the metal-MoS₂ contacts in two-dimensional field-effect transistors with atomic resolution

Ryan J. Wu,^{1,*} Sagar Udyavara,^{1,*} Rui Ma,² Yan Wang,³ Manish Chhowalla,^{3,4} Turan Birol,¹ Steven J. Koester,² Matthew Neurock,^{1,†} and K. Andre Mkhoyan^{1,‡}

¹*Department of Chemical Engineering and Materials Science, University of Minnesota, Minneapolis, Minnesota 55455, USA*

²*Department of Electrical and Computer Engineering, University of Minnesota, Minneapolis, Minnesota 55455, USA*

³*Department of Materials Science and Engineering, Rutgers University, Piscataway, New Jersey 08854, USA*

⁴*Department of Materials Science and Metallurgy, University of Cambridge, Cambridge CB3 0FS, United Kingdom*



(Received 27 April 2019; published 8 November 2019)

Two-dimensional MoS₂ is an excellent channel material for ultrathin field-effect transistors, but high contact resistance across the deposited metal-MoS₂ interface continues to limit its full realization. Using atomic-resolution scanning transmission electron microscopy and first-principles calculations, we showed that deposited metals with a high affinity for sulfur could have a fundamental limitation. Ti-MoS₂ contact shows a destruction of the MoS₂ layers, a formation of clusters and void pockets, and penetration of Ti into MoS₂, resulting in many localized pinning states in the band gap. InAu-MoS₂ contact shows that it is possible to achieve a van der Waals-type interface and dramatically reduced pinning states.

DOI: [10.1103/PhysRevMaterials.3.111001](https://doi.org/10.1103/PhysRevMaterials.3.111001)

Ultrathin field-effect transistors (FETs) using MoS₂ as the channel material have shown excellent performance, making them viable for sub-10-nm node devices [1–5]. However, the contact between the two-dimensional (2D) MoS₂ and an evaporated three-dimensional (3D) metal electrode remains a challenge due to the high contact resistance [6–9] attributed to the Fermi level pinning at the interface [10–13]. Although alternative approaches [9,14–19] to depositing the metal onto MoS₂ have been reported [20–22], including a direct metal film transfer which results in van der Waals (vdW) bonding [23,24], the origin of high contact resistance using evaporated metals remained unclear. Previous reports have attributed the Fermi level pinning to the formation of surface states created by adsorbed contaminants [25] or damage by kinetic energy transfer from metal deposition [23]. While these factors could play a role, they should be resolvable by improving the metal deposition. On the other hand, the actual bonding between a metal and MoS₂ layer is a more fundamental issue. The recent report by Wang *et al.* [26] shows that when In or In_xAu_y is used as the contact metal, low-resistant vdW contact can be achieved even with evaporated metal deposition. Therefore, understanding of the metal-MoS₂ interface from direct atomic-scale observations can be instrumental in mitigating Fermi level pinning.

To elucidate the structure of the metal-MoS₂ interface, we first studied deposited Ti contacts. In addition to Ti [12,13,27,28], other metals, such as Au, Pt, Ag, Sc, Pd, Ni, and Cu, were also used as the contact [4,23,27,29], but Ti provides a good case for a metal-MoS₂ interface with strong

bonds, as Ti possesses a very high affinity for sulfur (the Ti-S bond dissociation energy is 4.35 eV compared to Mo-S at 3.69 eV) [30]. We also studied the In_xAu_y-MoS₂ interface, where vdW-type bonding was reported [26]. Interfaces are studied using a combination of atomic-resolution scanning transmission electron microscopy (STEM) imaging with electron energy-loss spectroscopy (EELS). Density functional theory (DFT) calculations are carried out to further clarify the structural and electronic changes occurring at the deposited metal-MoS₂ interface.

The STEM specimens were prepared by focused ion beam (FIB) thinning of working FETs [see the Methods and Materials section, Fig. S1, in the Supplemental Material (SM) [31]] with characteristics similar to those reported in the literature [32,33]. Figures 1(a) and 1(b) show the schematic layout of the FETs and a low-magnification cross-sectional annular dark-field (ADF)-STEM image where the Au/Ti contact and Si/SiO₂ substrate bookend the MoS₂ layers (see SM Fig. S2 [31]). A high-magnification ADF-STEM image [Fig. 1(c)] shows that along the Ti-MoS₂ interface, there are areas where the Ti contacts the MoS₂ and alters the structure of the topmost layer. Next to these areas, small void pockets are visible which leaves the topmost MoS₂ layer pristine. While there are reports suggesting that Ti forms strong bonding with MoS₂ [25,28], this is a direct observation of (i) the degradation of the topmost MoS₂ layer and (ii) the presence of nm-size void pockets along the interface. The Ti atoms tend to not only bond but also cluster on the MoS₂ surface during deposition. Such Ti clustering behavior was predicted [25] but not observed experimentally (see SM Fig. S3 for additional images [31]). It should be noted that under the conditions of Ti deposition used here, there should be no damage to the MoS₂ layers.

An atomic-resolution ADF-STEM image [Fig. 1(d)] obtained from one of these Ti-clustered areas shows that the

*These authors contributed equally to this work.

†mneurock@umn.edu

‡mkhoyan@umn.edu

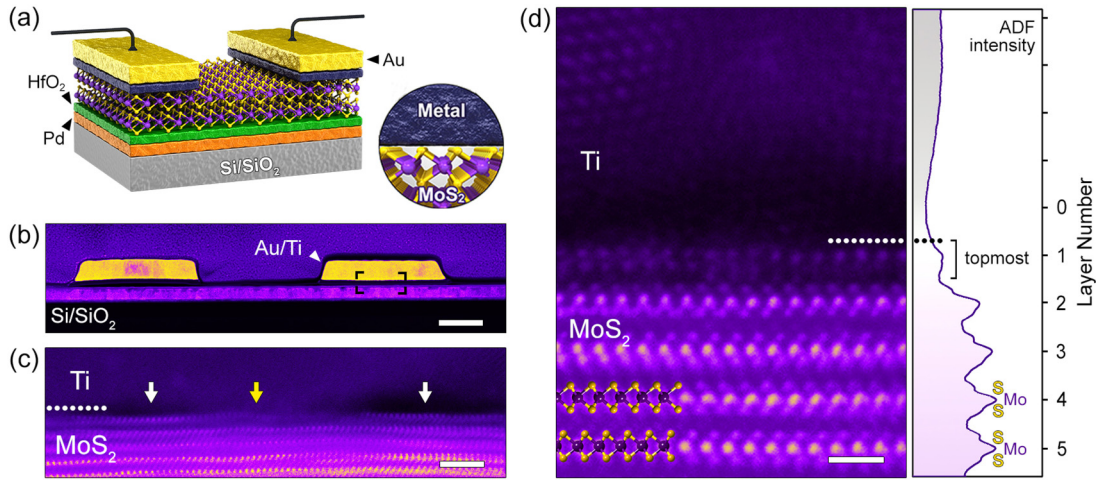


FIG. 1. (a) Schematic layout of the FET with MoS₂ channel and metal contacts. (b) Low-magnification cross-sectional ADF-STEM image of the FET. The protective amorphous C/Pt layers are also visible here. Scale bar is 0.2 μm . (c) High-magnification image of the Ti-MoS₂ interface from the boxed area in (b). An area where Ti is clustered is indicated by a yellow arrow and areas with void pockets by white arrows. Scale bar is 2 nm. (d) Atomic-resolution ADF-STEM image of the Ti-MoS₂ interface. The horizontally averaged ADF intensity is shown on the right. A ball-and-stick model of MoS₂ is overlaid on the image. Scale bar is 6 \AA .

topmost MoS₂ layer is degraded and barely identifiable. The compromised integrity of the topmost MoS₂ layer indicates that the bonding between Ti and S is strong enough to restructure the contacting MoS₂ layer. This Ti-driven restructuring of the topmost MoS₂ layer is far beyond the effects of carbon or oxide contaminants on the surface of the MoS₂ as (i) no degradation is observed in the sections of the MoS₂ layers under the void pockets which have the same level of contaminants, and (ii) in areas of the device not directly below the Ti contacts, the MoS₂ remains pristine (see SM Fig. S3 [31]). A slightly lower intensity of the ADF signal in the Ti region directly above the first MoS₂ layer is likely due to void pockets in the projection, or an nm-thick Ti sublayer with a lower atomic density, or both.

To measure the changes in the electronic structure of MoS₂ caused by the Ti contact, a layer-by-layer EELS analysis was performed. Core-level EELS edges measure localized changes in the element-specific electronic density of states (DOS) of the conduction band [34]. Figure 2(a) shows two $S L_{2,3}$ edges measured from the MoS₂ channel: one from layer 1, the topmost MoS₂ layer directly in contact with Ti, and from layer 5. The dominating features of the $S L_{2,3}$ fine structure, peaks I and II, composed of S 3s and 3d partial DOS [35], are different in these spectra. The peaks are more subdued in layer 1, which is consistent with the observed loss of crystallinity of the top MoS₂ layer [34]. Additional $S L_{2,3}$ edge EELS measurements from the MoS₂ not in contact with Ti showed

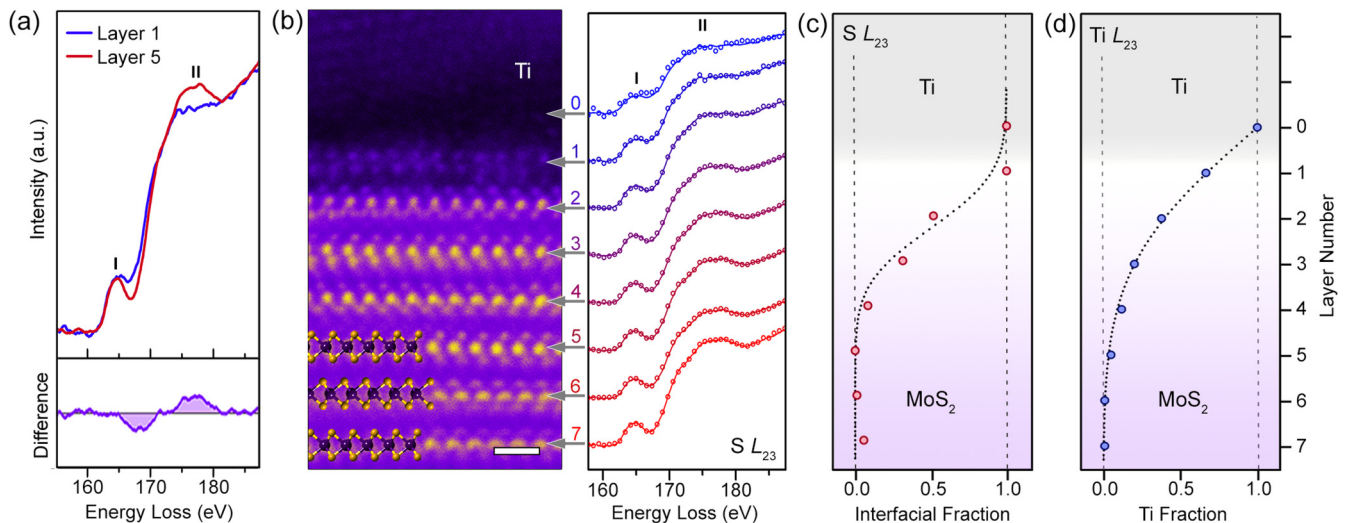


FIG. 2. (a) EELS $S L_{2,3}$ edges measured from the first (contacting to Ti) and the fifth MoS₂ layers. The differences between the two spectra are shown below. (b) Atomic-resolution ADF-STEM image of the MoS₂ layers (left) and EELS $S L_{2,3}$ edge measured from the layers (right). Scale bar is 5 \AA . Measured spectra are shown as scatter points and fitted spectra are shown as lines. (c) The fractions of the interfacial (layer 1) character in each $S L_{23}$ edge. (d) The fraction of Ti in MoS₂ layers. A $y = \text{erf}(x)$ fit through the data points in (c) and (d).

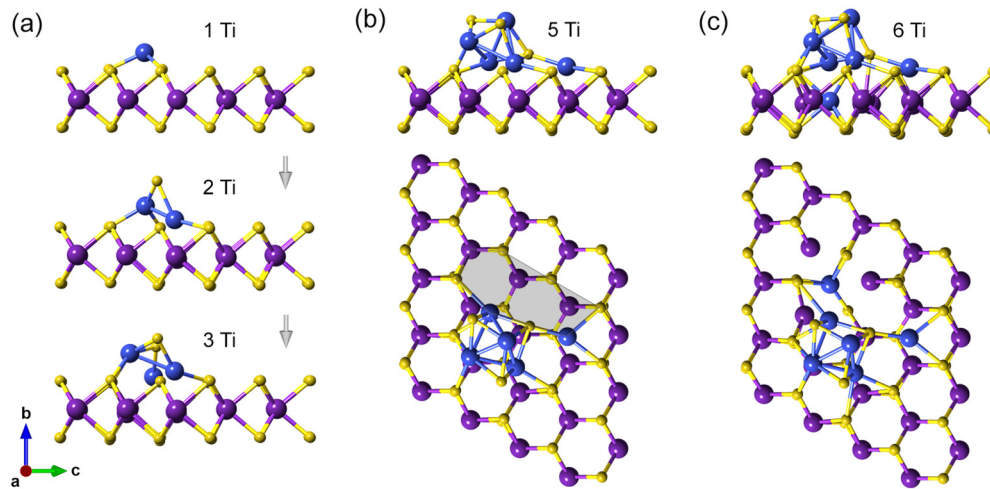


FIG. 3. (a) Models showing the lowest-energy optimized structures of the Ti-MoS₂ system following additions of one, two, and three Ti atoms (Mo, purple; S, yellow; Ti, blue). (b) Side view (above) and top view (below) of the Ti-MoS₂ system with five added Ti atoms. An opening in the MoS₂ layer is highlighted as the gray shaded region. (c) Side view (above) and top view (below) of the Ti-MoS₂ system showing the penetration of the sixth Ti atom into the opening highlighted in (b).

no differences between the first and fifth MoS₂ layers (see SM Fig. S4 [31]).

Figure 2(b) shows a set of core-level EELS measurements from each of the first seven MoS₂ layers and from the Ti contact layer directly above the MoS₂. Changes in peaks I and II of the S $L_{2,3}$ edge were quantified by fitting each spectrum to a linear superposition of the two reference spectra shown in Fig. 2(a) [36], and the fractions of the spectrum with interfacial and bulk characters were evaluated [Fig. 2(c)]. Layer 2 and even layer 3 of the MoS₂ have considerable interfacial character, indicating that the effects of the Ti contact go beyond the surface layer (for minor effects of probe broadening, see the Methods and Materials section in the SM [31]).

The presence of Ti atoms in deeper MoS₂ layers was also considered. The Ti $L_{2,3}$ edge was measured across the first seven MoS₂ layers [Fig. 2(d)]. Layers 2 and 3 also showed an appreciable amount of Ti present. The amounts of Ti present in layers 2 and 3 could be a factor in the observed changes in the fine structure of the S $L_{2,3}$ edge at these depths. However, they are not high enough to affect the pristine view of the atomic structure imaged in the projection [Fig. 1(d)].

DFT calculations were carried out to understand the interactions of Ti atoms with MoS₂ layers. In these simulations, individual Ti atoms were systematically added onto the surface of a monolayer MoS₂ to mimic experimental deposition. This “single-atom-addition” approach provides insight into the atomic processes occurring at the metal-MoS₂ interface during deposition, and complements the “metal-MoS₂-slab” approach [37–40], which models metal contacts directly transferred onto MoS₂ [23]. Simulations were performed without the effects of temperature and Ti atoms were added without kinetic energy (for details, see the Methods and Materials section in the SM [31]).

Figures 3(a) and 3(b) show the calculated lowest-energy structures of the Ti-MoS₂ interfaces after the addition of one to five Ti atoms. As will be clear later, a five-atom cluster of Ti was sufficient to explain the main STEM observations

discussed earlier. The interactions between the Ti and S are indeed strong enough to disrupt the MoS₂ by pulling S atoms out of the MoS₂ surface. Calculations also show the formation of a cluster, which degrades the pristine crystal structure of MoS₂. Furthermore, even with only five Ti atoms, a relatively large opening in the MoS₂ layer is formed [Fig. 3(b)]. This “nanopore” in the MoS₂ is large enough to allow the sixth Ti atom to penetrate and cause more structural modifications [Fig. 3(c)]. These results match with the experimentally observed structural degradation of the topmost MoS₂ layer and provide a pathway to how appreciable amounts of Ti could penetrate into the second and third layers of MoS₂. They also imply that the disruption of the MoS₂ crystal is inherent to Ti-MoS₂ bonding and cannot be avoided. Additional *ab initio* molecular dynamics (AIMD) calculations for the 5-Ti-atom cluster confirm its thermal stability at room temperature ($T = 300$ K) (see SM Video S1 [31]).

The electronic band structures and DOS for a pristine monolayer MoS₂ and for the MoS₂ with five bonded Ti atoms, shown in Fig. 3(c), were calculated (Fig. 4). As can be seen, a cluster of five Ti atoms will force the system to have many localized states in the band gap, some of which will act as pinning states for charge carriers. These band-gap states appear to be located on all three atomic species (Mo, S, and Ti) and likely pin the Fermi level at the interface [11,41]. The degradation of the crystallinity of the MoS₂ also results in the removal of degeneracies in the band structure and the flattening of the bands leading to dispersed DOS, which was observed in S $L_{2,3}$ EELS measurements [Fig. 2(a)].

The DFT calculations using the single-atom-addition approach were extended to other metals: Sc, Cu, Au, In, and In_xAu_y (Fig. 4). The results show that Sc, a transition metal as Ti, clusters and disrupts the MoS₂ layer. Both Sc and Ti disperse the valence and conduction bands and create a high number of pinning states in the band gap. In contrast, Cu and Au bind weakly to the surface sulfur and do not disrupt the structure of the MoS₂ layer. Their effects on the electronic band structure of MoS₂, including a number of new band-gap

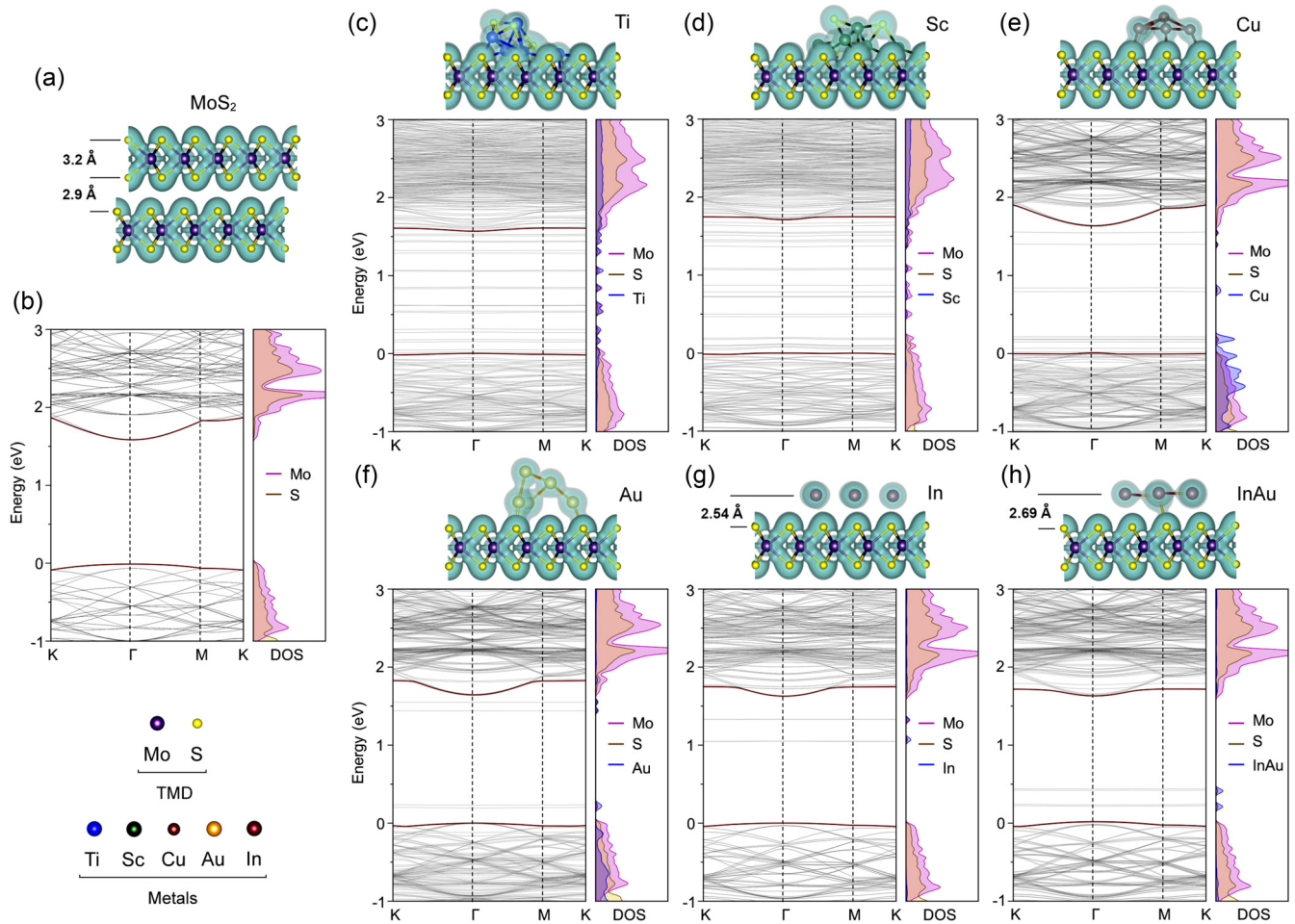


FIG. 4. (a) The atomic structure of bilayer MoS₂ with distances between sulfur layers indicated. (b) Electronic band structure and element-specific DOS for pristine monolayer MoS₂. (c)–(h) The atomic and electronic band structure of monolayer MoS₂ with five atoms of Ti, Sc, Cu, Au, In, and In_xAu_y (with three In and two Au). The charge densities for all structures are shown in transparent green on the top of the corresponding band structure. An isosurface value of 0.042 was chosen conservatively to ensure that the charge densities of the Cu atoms overlap. The minimum of the conduction band and maximum of the valence band are highlighted by maroon colors.

states, are also weaker. Of the metals studied, In and In_xAu_y are the least disruptive. The charge density plots in Fig. 4 show that In and In_xAu_y bind to MoS₂ through vdW-type bonds, and leave the MoS₂ structure intact (for the thermal stability of the 5-In-atom cluster at $T = 300$ K, see SM Video S2 [31]). This is also reflected in the electronic states, where the number of band-gap states introduced by In or In_xAu_y is very low. The calculations suggest that In or In_xAu_y should show minimum pinning and very low contact resistance, which is consistent with the measured low contact resistance in the FETs reported by Wang *et al.* [26]. In the case of the In_xAu_y alloy, In provides vdW-type bonding to MoS₂ with a very low number of gap states, while Au provides bonds with a light ionic character without considerably modifying the surface of MoS₂ and, therefore, low-barrier electron transition paths across the vdW gap. Due to similarities between the Au and Cu contacts to the MoS₂ layer [Figs. 4(e) and 4(f)], the In_xCu_y alloy could also be a good candidate for a low-cost, higher melting point metal with vdW-type low contact resistance. Calculations show that even in the presence of an S vacancy at the MoS₂ surface, In atoms bind with the vdW-type bond, while Ti atoms, as

before, disrupt the MoS₂ with strong Ti-S bonds (see SM Fig. S5 [31]).

STEM-EELS experiments were performed for the In_xAu_y–MoS₂ interface [26] to compare with the results of the DFT calculations based on the single-atom-addition approach. An atomic-resolution ADF-STEM image and corresponding EELS characterization of the MoS₂ layers are presented in Fig. 5. As can be seen, the In_xAu_y–MoS₂ contact is nondisruptive and the topmost MoS₂ layer appears completely intact. The distance between the top sulfur layer and the first atomic layer In_xAu_y is 2.7 ± 0.1 Å, which matches well with the DFT predicted distance of 2.69 Å. EELS measurements of the S $L_{2,3}$ edge show no detectable differences between spectra from layer 1, the topmost MoS₂ layer directly in contact with In_xAu_y, and the bulklike MoS₂ layer 5 [Fig. 5(b)], which is also consistent with the results of DFT calculations showing very minor changes in conduction band DOS.

In conclusion, the atomic-resolution STEM-EELS study of a metal-deposited metal–MoS₂ interface shows that for Ti the strength of the metal-sulfur interaction is sufficient to result

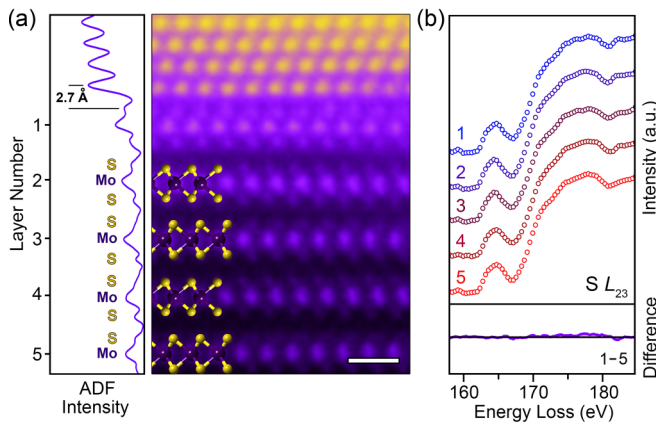


FIG. 5. (a) Atomic-resolution ADF-STEM image of the $\text{In}_x\text{Au}_y\text{-MoS}_2$ interface. The horizontally averaged ADF intensity is shown on the left. Scale bar is 5 Å. (b) EELS $S L_{2,3}$ edge measured from MoS_2 layers 1 to 5. The difference spectrum between the first (contacting to the In_xAu_y) and the fifth MoS_2 layers is shown below.

in the degradation of the surface MoS_2 layer, the penetration of Ti into deeper layers, the clustering of Ti atoms, and the

formation of void pockets, making the interface inhomogeneous. DFT calculations suggest such structural modifications of the metal- MoS_2 interface are inherent for systems where the metal has a very high affinity for sulfur (Ti, Sc, etc.). Band-structure calculations suggest that the Fermi level pinning in such systems is likely unavoidable. In contrast, for a metal with a low affinity for sulfur, such as In, the resulting interface can become vdW type. While the Fermi level pinning might still be present for a wide variety of metals, including Au or Cu, they can be dramatically mitigated with the proper selection of a metal or alloy, such as In, In_xAu_y , or In_xCu_y . Introduced here, the single-atom-addition approach in DFT calculations can be an effective method to evaluate the effects of deposited metals on MoS_2 and other layered materials.

The STEM analysis was performed in the Characterization Facility of the University of Minnesota, which receives partial support from the NSF through the MRSEC program. This project was partially supported by NSF MRSEC Program Grant No. DMR-1420013, the C-SPIN, one of the SRC STARnet centers, and SMART, one of seven centers of nCORE, a SRC program sponsored by NIST.

- [1] B. Radisavljevic, A. Radenovic, J. Brivio, V. Giacometti, and A. Kis, *Nat. Nanotechnol.* **6**, 147 (2011).
- [2] J. Shim, H.-Y. Park, D.-H. Kang, J.-O. Kim, S.-H. Jo, Y. Park, and J.-H. Park, *Adv. Electron. Mater.* **3**, 1600364 (2017).
- [3] M. Chhowalla, D. Jena, and H. Zhang, *Nat. Rev. Mater.* **1**, 16052 (2016).
- [4] S. Das, H.-Y. Chen, A. V. Penumatcha, and J. Appenzeller, *Nano Lett.* **13**, 100 (2013).
- [5] D. Jena, K. Banerjee, and G. H. Xing, *Nat. Mater.* **13**, 1076 (2014).
- [6] A. Allain, J. Kang, K. Banerjee, and A. Kis, *Nat. Mater.* **14**, 1195 (2015).
- [7] H. Liu, A. T. Neal, and P. D. Ye, *ACS Nano* **6**, 8563 (2012).
- [8] H. Liu, M. Si, S. Najmaei, A. T. Neal, Y. Du, P. M. Ajayan, J. Lou, and P. D. Ye, *Nano Lett.* **13**, 2640 (2013).
- [9] R. Kappera, D. Voiry, S. E. Yalcin, B. Branch, G. Gupta, A. D. Mohite, and M. Chhowalla, *Nat. Mater.* **13**, 1128 (2014).
- [10] J. Bardeen, *Phys. Rev.* **71**, 717 (1947).
- [11] C. Gong, L. Colombo, R. M. Wallace, and K. Cho, *Nano Lett.* **14**, 1714 (2014).
- [12] C. Kim, I. Moon, D. Lee, M. S. Choi, F. Ahmed, S. Nam, Y. Cho, H.-J. Shin, S. Park, and W. J. Yoo, *ACS Nano* **11**, 1588 (2017).
- [13] Y. Du, L. Yang, H. Liu, and P. D. Ye, *APL Mater.* **2**, 092510 (2014).
- [14] M. H. D. Guimarães, H. Gao, Y. Han, K. Kang, S. Xie, C.-J. Kim, D. A. Muller, D. C. Ralph, and J. Park, *ACS Nano* **10**, 6392 (2016).
- [15] X. Cui, E.-M. Shih, L. A. Jauregui, S. H. Chae, Y. D. Kim, B. Li, D. Seo, K. Pistunova, J. Yin, J.-H. Park, H.-J. Choi, Y. H. Lee, K. Watanabe, T. Taniguchi, P. Kim, C. R. Dean, and J. C. Hone, *Nano Lett.* **17**, 4781 (2017).
- [16] J. Wang, Q. Yao, C.-W. Huang, X. Zou, L. Liao, S. Chen, Z. Fan, K. Zhang, W. Wu, X. Xiao, C. Jiang, and W.-W. Wu, *Adv. Mater.* **28**, 8302 (2016).
- [17] N. Kaushik, D. Karmakar, A. Nipane, S. Karande, and S. Lodha, *Appl. Mater. Interfaces* **8**, 256 (2016).
- [18] L. Yu, Y.-H. Lee, X. Ling, E. J. G. Santos, Y. C. Shin, Y. Lin, M. Dubey, E. Kaxiras, J. Kong, H. Wang, and T. Palacios, *Nano Lett.* **14**, 3055 (2014).
- [19] K. Cho, J. Pak, J.-K. Kim, K. Kang, T.-Y. Kim, J. Shin, B. Y. Choi, S. Chung, and T. Lee, *Adv. Mater.* **30**, 1705540 (2018).
- [20] S.-S. Chee, D. Seo, H. Kim, H. Jang, S. Lee, S. P. Moon, K. H. Lee, S. W. Kim, H. Choi, and M.-H. Ham, *Adv. Mater.* **31**, 1804422 (2019).
- [21] L. Xie, M. Liao, S. Wang, H. Yu, L. Du, J. Tang, J. Zhao, J. Zhang, P. Chen, X. Lu, G. Wang, G. Xie, R. Yang, D. Shi, and G. Zhang, *Adv. Mater.* **29**, 1702522 (2017).
- [22] Y. Liu, H. Wu, H.-C. Cheng, S. Yang, E. Zhu, Q. He, M. Ding, D. Li, J. Guo, N. O. Weiss, Y. Huang, and X. Duan, *Nano Lett.* **15**, 3030 (2015).
- [23] Y. Liu, J. Guo, E. Zhu, L. Liao, S.-J. Lee, M. Ding, I. Shakir, V. Gambin, Y. Huang, and X. Duan, *Nature (London)* **557**, 696 (2018).
- [24] Y. Liu, Y. Huang, and X. Duan, *Nature (London)* **567**, 323 (2019).
- [25] S. McDonnell, C. Smyth, C. L. Hinkle, and R. M. Wallace, *ACS Appl. Mater. Interfaces* **8**, 8289 (2016).
- [26] Y. Wang, J. C. Kim, R. J. Wu, J. Martinez, X. Song, J. Yang, F. Zhao, A. Mkhoyan, H. Y. Jeong, and M. Chhowalla, *Nature (London)* **568**, 70 (2019).
- [27] C. M. Smyth, R. Addou, S. McDonnell, C. L. Hinkle, and R. M. Wallace, *J. Phys. Chem. C* **120**, 14719 (2016).
- [28] C. D. English, G. Shine, V. E. Dorgan, K. C. Saraswat, and E. Pop, *Nano Lett.* **16**, 3824 (2016).

- [29] C. Gong, C. Huang, J. Miller, L. Cheng, Y. Hao, D. Cobden, J. Kim, R. S. Ruoff, R. M. Wallace, K. Cho, X. Xu, and Y. J. Chabal, *ACS Nano* **7**, 11350 (2013).
- [30] Y.-R. Luo, *Comprehensive Handbook of Chemical Bond Energies*, 1st ed. (CRC Press, Boca Raton, FL, 2007).
- [31] See Supplemental Material at <http://link.aps.org/supplemental/10.1103/PhysRevMaterials.3.111001> for a description of the experimental and computational parameters and methods, data analysis, evaluation of beam broadening, and supplemental figures, tables, and videos, which includes Refs. [32,33,42–62].
- [32] W. Liu, J. Kang, W. Cao, D. Sarkar, Y. Khatami, D. Jena, and K. Banerjee, in *2013 IEEE International Electron Devices Meeting (IEDM)* (IEEE, Piscataway, NJ, 2013), pp. 19.4.1–19.4.4.
- [33] C. U. Kshirsagar, W. Xu, Y. Su, M. C. Robbins, C. H. Kim, and S. J. Koester, *ACS Nano* **10**, 8457 (2016).
- [34] R. F. Egerton, *Electron Energy-Loss Spectroscopy in the Electron Microscope*, 3rd ed. (Springer, New York, 2011).
- [35] M. Dadsetani, H. Nejatipour, and T. Nouri, *Physica E* **73**, 198 (2015).
- [36] D. A. Muller, T. Sorsch, S. Moccio, F. H. Baumann, K. Evans-Lutterodt, and G. Timp, *Nature (London)* **399**, 758 (1999).
- [37] J. Kang, W. Liu, D. Sarkar, D. Jena, and K. Banerjee, *Phys. Rev. X* **4**, 031005 (2014).
- [38] I. Popov, G. Seifert, and D. Tománek, *Phys. Rev. Lett.* **108**, 156802 (2012).
- [39] J. Kang, D. Sarkar, W. Liu, D. Jena, and K. Banerjee, in *2012 International Electron Devices Meeting (IEDM)*, (IEEE, Piscataway, NJ, 2012), pp. 17.4.1–17.4.4.
- [40] H. Zhong, R. Quhe, Y. Wang, Z. Ni, M. Ye, Z. Song, Y. Pan, J. Yang, L. Yang, M. Lei, J. Shi, and J. Lu, *Sci. Rep.* **6**, 21786 (2016).
- [41] K. Sotthewes, R. van Bremen, E. Dollekamp, T. Boulogne, K. Nowakowski, D. Kas, H. J. W. Zandvliet, and P. Bampoulis, *J. Phys. Chem. C* **123**, 5411 (2019).
- [42] K. M. Freedy, A. Giri, B. M. Foley, M. R. Barone, P. E. Hopkins, and S. McDonnell, *Nanotechnology* **29**, 145201 (2018).
- [43] R. F. Bunshah, *Handbook of Deposition Technologies for Films and Coatings: Science, Technology, and Applications* (William Andrew, Oxford, UK, 1994).
- [44] *Brazing Manual*, 3rd ed. (American Welding Society, Miami, FL, 1976).
- [45] H.-P. Komsa, J. Kotakoski, S. Kurasch, O. Lehtinen, U. Kaiser, and A. V. Krasheninnikov, *Phys. Rev. Lett.* **109**, 035503 (2012).
- [46] K. D. Dorfman and P. Daoutidis, *Numerical Methods with Chemical Engineering Applications* (Cambridge University Press, Cambridge, UK, 2017).
- [47] E. J. Kirkland, *Advanced Computing in Electron Microscopy*, 2nd ed. (Springer, New York, 2010).
- [48] R. J. Wu, A. Mittal, M. L. Odlyzko, and K. A. Mkhoyan, *Microsc. Microanal.* **23**, 794 (2017).
- [49] J. L. Feldman and L. L. Boyer, *Solid State Commun.* **37**, 879 (1981).
- [50] A. Mittal, D. B. Zhang, C. Teresi, T. Dumitrica, and K. A. Mkhoyan, *Phys. Rev. B* **84**, 153401 (2011).
- [51] P. A. Young, *J. Phys. D: Appl. Phys.* **1**, 936 (1968).
- [52] G. Kresse and J. Hafner, *Phys. Rev. B* **47**, 558(R) (1993).
- [53] G. Kresse and J. Hafner, *Phys. Rev. B* **49**, 14251 (1994).
- [54] G. Kresse and J. Furthmüller, *Comput. Mater. Sci.* **6**, 15 (1996).
- [55] G. Kresse and J. Furthmüller, *Phys. Rev. B* **54**, 11169 (1996).
- [56] J. P. Perdew, K. Burke, and M. Ernzerhof, *Phys. Rev. Lett.* **77**, 3865 (1996).
- [57] G. Kresse and D. Joubert, *Phys. Rev. B* **59**, 1758 (1999).
- [58] P. Blöchl, O. Jepsen, and O. Andersen, *Phys. Rev. B* **49**, 16223 (1994).
- [59] A. R. Puigdollers, P. Schlexer, and G. Pacchioni, *J. Phys. Chem. C* **119**, 15381 (2015).
- [60] P. Schlexer and G. Pacchioni, *J. Phys. Chem. C* **121**, 14717 (2017).
- [61] S. Grimme, *J. Comput. Chem.* **27**, 1787 (2006).
- [62] J. A. Wilson and A. D. Yoffe, *Adv. Phys.* **18**, 193 (1969).